



**HAL**  
open science

## Microscopic correlation between chemical and electronic states in epitaxial graphene on SiC ( $000\bar{1}$ )

C. Mathieu, N. Barrett, J. Rault, Y. Y. Mi, B. Zhang, W. A. de Heer,  
Clément Berger, E. H. Conrad, O. Renault

► **To cite this version:**

C. Mathieu, N. Barrett, J. Rault, Y. Y. Mi, B. Zhang, et al.. Microscopic correlation between chemical and electronic states in epitaxial graphene on SiC (  $000\bar{1}$  ). Physical Review B: Condensed Matter and Materials Physics (1998-2015), 2011, 83, pp.235436. 10.1103/PhysRevB.83.235436 . cea-01481024

**HAL Id: cea-01481024**

**<https://cea.hal.science/cea-01481024>**

Submitted on 2 Mar 2017

**HAL** is a multi-disciplinary open access archive for the deposit and dissemination of scientific research documents, whether they are published or not. The documents may come from teaching and research institutions in France or abroad, or from public or private research centers.

L'archive ouverte pluridisciplinaire **HAL**, est destinée au dépôt et à la diffusion de documents scientifiques de niveau recherche, publiés ou non, émanant des établissements d'enseignement et de recherche français ou étrangers, des laboratoires publics ou privés.

**Microscopic correlation between chemical and electronic states in epitaxial graphene on SiC(000 $\bar{1}$ )**

C. Mathieu

*IRAMIS/SPCSI/LENSIS, F-91191 Gif-sur-Yvette, France and CEA, LETI, MINATEC Campus, F-38054 Grenoble Cedex 09, France*

N. Barrett,\* J. Rault, and Y. Y. Mi

*IRAMIS/SPCSI/LENSIS, F-91191 Gif-sur-Yvette, France*

B. Zhang and W. A. de Heer

*The Georgia Institute of Technology, Atlanta, Georgia 30332-0430, USA*

C. Berger

*The Georgia Institute of Technology, Atlanta, Georgia 30332-0430, USA and CNRS/Institut Néel, BP166, F-38042 Grenoble, France*

E. H. Conrad

*The Georgia Institute of Technology, Atlanta, Georgia 30332-0430, USA*

O. Renault

*CEA, LETI, MINATEC Campus, F-38054 Grenoble Cedex 09, France*

(Received 6 April 2011; revised manuscript received 26 May 2011; published 30 June 2011)

We present energy filtered electron emission spectromicroscopy with spatial and wave-vector resolution on few-layer epitaxial graphene on SiC(000 $\bar{1}$ ) grown by furnace annealing. Low-energy electron microscopy shows that more than 80% of the sample is covered by 2–3 graphene layers. C1s spectromicroscopy provides an independent measurement of the graphene thickness distribution map. The work function, measured by photoelectron emission microscopy (PEEM), varies across the surface from 4.34 to 4.50 eV according to both the graphene thickness and the graphene-SiC interface chemical state. At least two SiC surface chemical states (i.e., two different SiC surface structures) are present at the graphene/SiC interface. Charge transfer occurs at each graphene/SiC interface.  $k$ -space PEEM gives 3D maps of the  $|\bar{k}_{\parallel}| \pi$ - $\pi^*$  band dispersion in micron-scale regions showing that the Dirac point shifts as a function of graphene thickness. Bragg diffraction of the Dirac cones via the superlattice formed by the commensurately rotated graphene sheets is observed. The experiments underline the importance of lateral and spectroscopic resolution on the scale of future electronic devices in order to precisely characterize the transport properties and band alignments.

DOI: [10.1103/PhysRevB.83.235436](https://doi.org/10.1103/PhysRevB.83.235436)

PACS number(s): 73.22.Pr, 61.48.Gh, 79.60.–i

**I. INTRODUCTION**

With the demonstration of GHz FETs based on epitaxial graphene grown on SiC,<sup>1,2</sup> this material has become the leading candidate for graphene-based electronics. Nonetheless, exploiting the remarkable properties of graphene for carbon based electronics remains an important challenge. The band structure and transport properties of graphene must be either preserved or modified in a reproducible fashion on typical device scales. While a good deal of work has already focused on monolayer graphene grown on the SiC(0001) (Si face),<sup>3</sup> the ability to grow thin graphene films on the SiC(000 $\bar{1}$ ) (C face) has only recently been demonstrated.<sup>4</sup> C-face films offer a particular advantage because of their rotational stacking that effectively decouples adjacent graphene layers.<sup>5,6</sup> This leads to very high mobilities<sup>7,8</sup> and allows devices to be less sensitive to thickness variations. While these systems continue to make progress toward realistic carbon electronics, significant research problems remain. One in particular is the study and control of the graphene-SiC interface.

When graphene is grown on the Si-terminated SiC on SiC(0001) (Si face), the first graphene layer grows on an insulating carbon buffer layer with a  $(6\sqrt{3} \times 6\sqrt{3})R30^\circ$

symmetry.<sup>9</sup> This buffer layer has a graphene structure and can be isolated from the SiC by intercalating hydrogen between the SiC substrate and the buffer layer.<sup>10</sup> However, mobilities in this isolated buffer layer remain low suggesting either some type of prior disorder in the layer before hydrogenation or an effect caused by the hydrogenation itself. Very little is known about the C-terminated SiC(000 $\bar{1}$ ) graphene-SiC interface. However, it is known that the C-face and Si-face interfaces must be very different.<sup>11</sup> X-ray studies show that the atomic density gradient at the interface is different for Si face and C face,<sup>12,13</sup> and core level photoelectron spectroscopy shows clear differences between the two interfaces.<sup>14</sup> Also, unlike the Si face, the C-face interface is known to have two coexisting structures (at least in the early growth phase). Scanning tunneling microscopy (STM) studies have shown that, in UHV growth conditions, poorly ordered  $(2 \times 2)$  and  $(3 \times 3)$  surface reconstructions exist below the first graphene layer.<sup>15</sup> However, these structures may become disordered or simply not exist when growth occurs at higher temperatures. In high-temperature furnace growth, there is no real evidence that the interface has a reconstruction. It is either an ordered  $(1 \times 1)$  or a disordered reconstruction. The most important observation demonstrating that the C-face interface is very different from

the Si face is that C-face graphene has a rotational stacking very different from that of Si-face graphene even when growth temperatures are the same.<sup>5,6,9</sup> This implies that the registry forces, and thus the interfaces, must be different on the two surfaces. Finally the rapid growth of C-face graphene at temperatures lower than those observed on the Si face point to a significant difference in the chemistry of the interface.<sup>9</sup>

In this work we present a detailed study of the C-face graphene-SiC interface. To date, most of the experimental techniques used to study the atomic and electronic structure are area averaged and are therefore not sensitive to variations on the micron scale. Near-field methods such as scanning tunneling microscopy (STM) can reduce the probed area by two orders of magnitude. However STM does not probe the interface itself and still provides very little information on the intervening length scales, which are precisely those of interest in many potential device applications. Recently this intermediate length scale has begun to be explored using low-energy electron microscopy (LEEM). Luxmi *et al.*<sup>16</sup> have studied the morphology of both UHV and argon furnace growth C-face graphene. Their work revealed a great deal of graphene thickness variation in these thick argon grown films.

We focus on the spatial variation of both the electronic structure and chemical bonding of the C-face graphene-SiC interface. The studies were carried out on thin C-face graphene films grown by a controlled Si sublimation technique. In particular, we investigate the chemical homogeneity of the interface, and correlate it with changes in doping, the graphene work function, and graphene's 2D band structure near the Fermi level. We show that the interface is very complicated with local chemical changes that are not all associated with the local graphene thickness. To carry out these studies, we use LEEM, photoemission electron microscopy (PEEM), and x-ray photoemission electron microscopy (X-PEEM). In addition, by using a suitable lens configuration the focal (or diffraction) plane of the PEEM can be imaged to give parallel momentum resolved dispersion curves  $E(k_x, k_y)$ . This technique is known as  $k$ -resolved photoemission electron microscopy ( $k$ -PEEM). Imaging the focal plane in PEEM produces a map for all azimuths simultaneously. Conservation of the component of the electron wave vector parallel to the sample surface automatically transforms this map into one of photoelectron intensity as a function of  $(k_x, k_y)$ , which is a horizontal cut in reciprocal space. Combined with energy analysis, this produces an image in reciprocal space of the local intensity as a function of the wave vector parallel to the surface. For example, the Fermi surface can be acquired in a single-shot experiment.<sup>17</sup>

## II. EXPERIMENT

The substrate used in these studies was a 6H conducting SiC(000 $\bar{1}$ ) from Cree, Inc. Before graphene growth, the sample was first H<sub>2</sub> etched for 30 min at 1400 °C. The sample was then grown in an enclosed graphite RF furnace using the confinement controlled sublimation process, CCS.<sup>4</sup> The growth was done at 1475 °C for 20 min.

Before all measurements, the sample was annealed at 500 °C for 1 minute in UHV to remove surface contamination. The surface cleanliness was checked by Auger electron

spectroscopy and x-ray photoemission (XPS). LEEM was used to quantify the graphene-layer thickness. LEEM experiments were carried out using a commercial Elmitec PEEM/LEEM III with base pressure of  $4 \times 10^{-8}$  Pa. The energy filtered X-PEEM experiments were conducted on the TEMPO beamline of the SOLEIL synchrotron (Saint Aubin, France) using a NanoESCA X-PEEM (Omicron Nanotechnology GmbH).<sup>18,19</sup> A double-pass hemispherical energy analyzer was used to compensate single-analyzer aberrations. This resulted in a PEEM energy resolution of 0.2 eV with a lateral resolution of  $\sim 100$  nm for core level emission. Experiments were conducted in ultrahigh vacuum (UHV) at a pressure of  $6 \times 10^{-9}$  Pa.

The X-PEEM image series was acquired over the photoemission threshold region and the C1s core level ( $h\nu = 654.3$  eV). A  $53 \mu\text{m}$  field of view (FoV) was used with 12 kV extraction voltage. For the real-space PEEM mode (threshold and C1s), a contrast aperture of  $70 \mu\text{m}$  was used; the lateral resolution was estimated to be 100 nm. The analyzer entrance slit was set to 0.5 mm with a 100 eV pass energy to give a resolution of 200 meV. The resolving power of the TEMPO beamline is approximately 5000, giving an overall estimated energy resolution better than 250 meV. Dark images were acquired with the MCP turned off in order to remove camera noise. Flat-field images were acquired to correct for MCP defects. The parabolic non-isochromaticity of the instrument was corrected for all images.<sup>19</sup>

The  $k$ -PEEM results were acquired using the same incident x-ray spot position on the sample as the X-PEEM analysis (beam size  $\sim 100 \mu\text{m} \times 50 \mu\text{m}$  provides uniform illumination). Because of the high extraction voltage between the sample and the lens, the wave vector resolution and the dimensions of the reciprocal-space image are independent of the photon energy for the typical spectral ranges used in these experiments. The lateral spatial resolution in the  $k$ -PEEM mode was purposefully reduced by operating with a full open aperture. This was required to image a sufficient portion of reciprocal space in order to cover a full Brillouin zone. In this setup, the area of interest on the sample surface is chosen by a field aperture situated in an intermediate image plane that was closed down to about  $7 \mu\text{m}$ . A transfer lens then projected the  $1500 \mu\text{m}$  diameter disk of the focal plane via the energy analyzer onto the detector giving a 2D  $k$ -space dimension of about  $\pm 2.5 \text{ \AA}^{-1}$  around the  $\Gamma$  point. The spectrometer resolution was 200 meV, the photon bandwidth 20 meV, and the wave-vector resolution  $\sim 0.05 \text{ \AA}^{-1}$ . The detector response was corrected by the flat field of the detector and camera defects were eliminated using dark images. Operating this way gave a  $\sim 1 \mu\text{m}$  lateral resolution for the band structure imaging.

## III. RESULTS

While Si-face graphene is known to grow oriented  $30^\circ$  relative to the principle SiC(21 $\bar{3}$ 0) direction, multilayer C-face graphene is known to be stacked with sheets within the stack having multiple rotation angles peaked at  $30^\circ$  and  $0^\circ \pm \sim 7^\circ$ . These C-face graphene rotations are due to interleaved rotated graphene sheets with non-Bernal stacking (i.e., non- $60^\circ$  rotations). In thin C-face samples there are only a few rotations. This is demonstrated in the LEED patterns in Fig. 1.

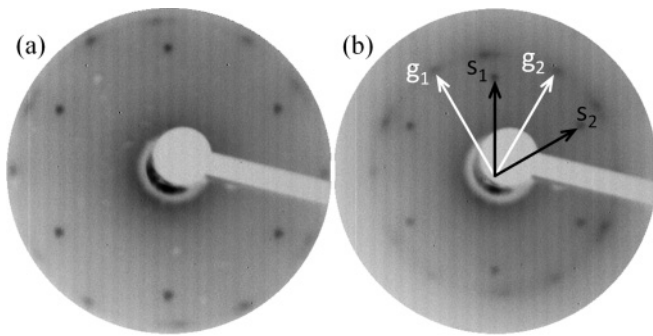


FIG. 1. LEED patterns from a nominally 3-layer C-face graphene sample with primary electron energy of (a) 76 eV and (b) 126 eV.

Because the films are thin, the LEED pattern clearly shows the sixfold SiC substrate spots ( $S_1$  and  $S_2$ ). In addition, the LEED shows a set of graphene spots rotated by  $30^\circ$  with respect to the  $S_2$  ( $g_1$  and  $g_2$ ) and a second set of spots rotated  $\sim 4^\circ-5^\circ$  relative to  $S_2$ . Weaker graphene arcs around  $0^\circ$  are also visible. The SiC substrate LEED pattern is  $1 \times 1$  and no additional diffraction spots that would suggest that a significant reconstruction is visible. However, these LEED images are macroscopic area-averaged results, and are not expected to be sensitive to microscopic variations in the interface structure. More detailed spatial information is obtained using LEEM and X-PEEM as discussed below.

**A. LEEM**

LEEM data were obtained by using the (0,0) specular backscattered electron beam. Figure 2 shows typical bright-field images with a FoV of  $10 \mu\text{m}$  for electron energies ( $E$ ) of 3.0 and 4.8 eV. A full image series was acquired by varying  $E$  from 1.5 to 12.9 eV (using a 50 meV step size). The low-energy onset of the backscattered electron signal depends on the potential just above the surface and thus on the local work function. Clear differences in contrast as a function of  $E$  are observed across the field of view suggesting distinct work functions for different regions of the surface.

In two-dimensional layered systems there are oscillations in the LEEM reflectivity at low electron energies.<sup>20-22</sup> Several groups have used these reflectivity oscillations to determine the number of graphene layers in the epitaxial film. Figure 2(c)

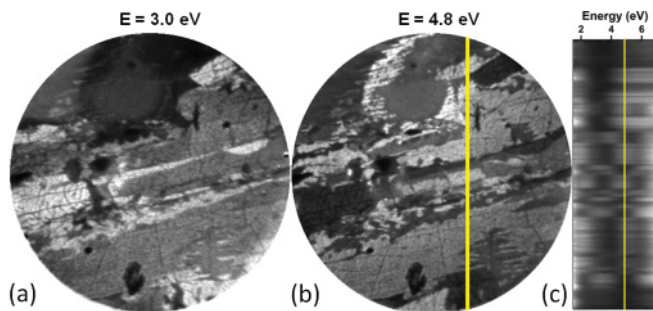


FIG. 2. (Color online) (a)–(c) Typical LEEM images ( $10 \mu\text{m}$  FoV) of the graphene surface as a function of electron energy (a) 3.0 eV and (b) 4.8 eV. (c) Reflectivity spectra extracted along the dotted line in (b) showing clearly the variation in the number of intensity minima and therefore the number of graphene layers.

shows the spectra along the dotted line in Fig. 2(b). We observe oscillations between 1.5 and about 7.5 eV. In graphite there are band gaps below 0 eV and above 7 eV along the  $\Gamma A$  direction. In an ideal multilayer graphene film, the number of minima in the reflectivity between successive Bragg peaks gives directly the number of graphene layers. We have similarly extracted pixel-by-pixel reflectivity curves from the image stack and mapped the LEEM reflectivity across the  $10 \mu\text{m}$  FoV and used the number of minima in each reflectivity curve to produce a thickness map of the C-face graphene film. Figure 3(a) shows the typical reflectivity curves for each distinct contrast region in the FoV. Two slightly different curves without a clear oscillation between 1.5 and 7 eV are observed. They are both attributed to the zero'th layer or C-terminated layer of the SiC substrate. This layer is thought to interact strongly with the SiC substrate through  $sp^3$  bonding. Luxmi *et al.*<sup>16</sup> have shown even flatter reflectivity curves for the zero'th layer (0 ML) for surfaces prepared at higher temperature under an argon back pressure. The thickness map constructed from the intensity minima is shown in Fig. 3(b) using the same color coding. The data show that more than 80% of the surface is covered by 2- or 3-layer graphene.

The reflectivity oscillation can be understood as quantum interference between electrons reflected by different graphene layers.<sup>20</sup> Hibino *et al.*<sup>20</sup> pointed out that although the conduction band is continuous in bulk graphite between 4.3 and

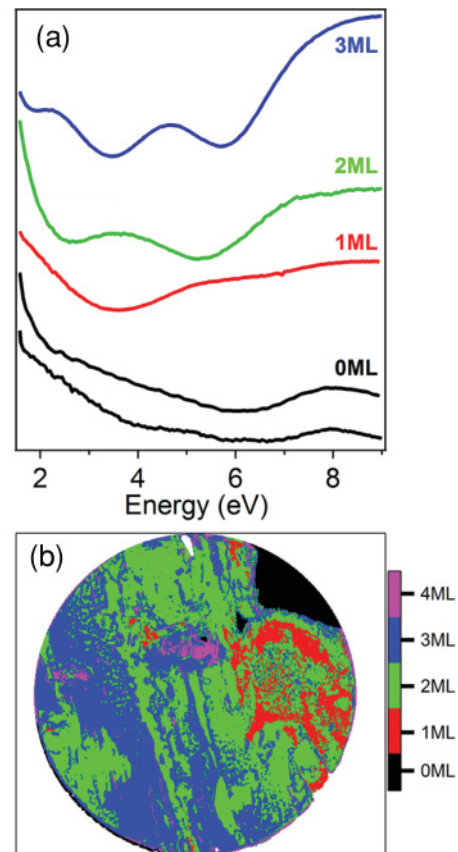


FIG. 3. (Color online) (a) Typical reflectivity curves extracted from the LEEM data set showing 0 to 3 oscillations below 7.5 eV. (b) Graphene thickness map (FoV =  $10 \mu\text{m}$ ) generated by counting the number of minima in the reflectivity curves.

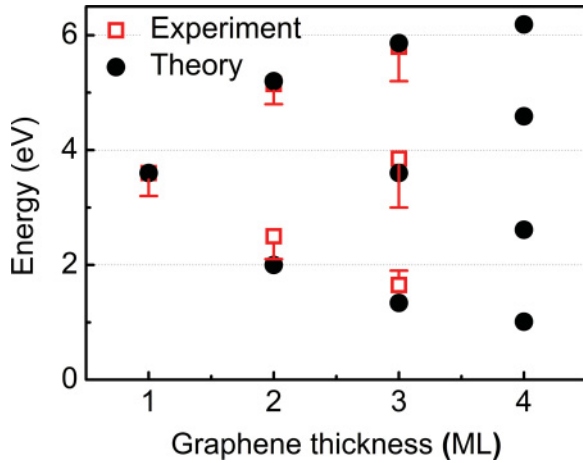


FIG. 4. (Color online) The position (boxes) of dips in reflectivity curves from Fig. 2(c) and Fig. 3(a), compared with theoretical estimation based on tight-binding model ( $\bullet$ ). The error bar on the experimental data indicates the correlations between the spread in the energy of the reflectivity minima.

11 eV along  $\Gamma A$ , few-layer graphene should have discrete states; thus the reflectivity oscillations are correlated with the electron structure of the thin films. The quantized conduction band states enhance the transmission of the incident electrons producing the dips in the reflectivity curves. This is confirmed by the good agreement between the experimental minima positions and the resonant energies predicted by a tight-binding calculation. For an  $m$ -layer thin film the bulk band dispersion has discrete energy states when the wave vector satisfies the quantized condition  $E = \epsilon - 2t \cos K\alpha$ , where  $\epsilon$  is the energy of the band center,  $t$  is the transfer integral, and  $\alpha$  is the interlayer distance. At these values, the dips in the reflectivity are predicted by projecting the wave vector onto the calculated band structure along the  $\Gamma A$  direction, the normal to the graphene layers.

Figure 4 shows the comparison of experimental reflectivity minima with the discrete energy levels predicted by the tight-binding theory. The spread in the experimental energy of the reflectivity minima in different regions of the FoV is indicated as an error bar. The center energy of the tight-binding theory calculation is at 3.6 eV compared to 3 eV used by Hibino for Si-face graphene.<sup>20</sup> Note that the third calculated

minimum (highest energy) in the nominally 3 ML region is at a slightly higher energy whereas the first and second minima are at slightly lower energy than the experimental data. This trend is also seen in the 2 ML minima. The difference may be due to the approximations inherent in the tight-binding calculation.

## B. X-PEEM

While LEEM measurements give information on the structural spatial variation of the graphene thickness, lateral variations in the electronic structure of epitaxial graphene have never been mapped. X-PEEM offers a unique method to begin to understand the role the SiC-graphene interface plays in graphene's electronic structure. In this section we present a submicron chemical and electronic mapping of the graphene-SiC interface.

### I. Work function

Probing the transition from the mirror reflection of the electrons to the backscattering regime, commonly referred to as mirror electron microscopy to low-energy electron microscopy (MEM-LEEM), one finds that it is highly sensitive to the local variations of the electric potential just above the surface, as small differences in the latter determine large differences in the electron reflectivity. In energy-filtered PEEM, at high photon energies (654.3 eV in these experiments), the photoemitted intensity at threshold is directly related to the work function. An example of a raw image obtained in the threshold region is shown in Fig. 5(a). As  $E - E_F$  is scanned, dark areas become bright and vice versa, giving rise to spatial contrast as a function of photoelectron kinetic energy. This is direct evidence for a distribution of work function values over the sample surface.

After correction for the Schottky effect due to the high extractor field,  $\Delta E = 98$  meV for 12 kV,<sup>23</sup> the photoemission threshold spectra can be used to directly measure the local work function. The threshold spectrum is extracted from each pixel in the FoV (pixel area  $65 \times 65$  nm<sup>2</sup>). The position of the threshold is obtained from a fit using a complementary error function,

$$I(E) = A \operatorname{erfc} \left( \frac{\Phi_{WF} - E}{\sqrt{2}\sigma} \right) + I_{\min}, \quad (1)$$

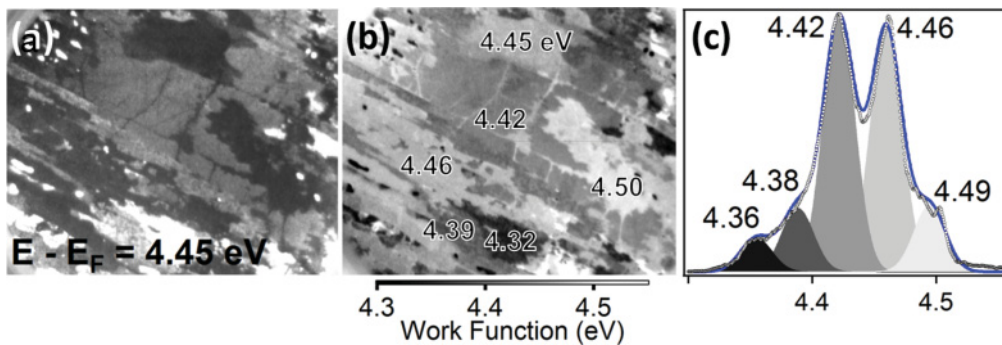


FIG. 5. (Color online) (a) Threshold image at  $E - E_F = 4.45$  eV with a  $53 \mu\text{m}$  field of view showing clear intensity contrast due to work function variation across the surface. (b) Work function map of the FoV obtained from a pixel by pixel analysis of the threshold spectra. (c) Histogram of the work function values in (b) showing five distinct Gaussian distributions, corresponding to five distinct work function values.

where  $\Phi_{WF}$  is the work function and  $\sigma$  the half-width of the rising side of the secondary electron peak (0.1 eV here). We note that because the theoretical shape of the photoemission onset is modeled, this method is a more reliable way of obtaining absolute work function values than simply extrapolating a straight line down to zero intensity. The results of this analysis are presented in the form of a map of the work function within the field of view in Fig. 5(b). A histogram of the work function values across the whole FoV is shown in Fig. 5(c). Five Gaussians, with width  $\pm 25$  meV, are able to describe the work function frequency distribution suggesting that there are only five distinct values of the work function. Actually, as we show when we discuss the X-PEEM results, the peak in the work function distribution centered at 4.46 eV includes two slightly different different work functions ( $\Delta\Phi = 10$  meV). While these two regions of the surface have nearly the same work function they can be distinguished by their very different core level spectra.

The work function distribution spans a range from 4.34 eV to 4.50 eV, a range well below the work function of bulk graphite (4.6 eV); thus our results confirm that no significant part of the surface within the FoV consists of many-layer graphene or graphite. On the contrary, this epitaxial film is indeed nearly uniform few-layer graphene, with local variations in the graphene coverage. However, we cannot necessarily attribute each peak in the work function distribution to a distinct graphene thickness. For example, recent Kelvin force microscopy showed that the work function difference between one- and two-layer graphene is 0.135 eV.<sup>24</sup> The graphene thickness calibration, based on the local C1s X-PEEM spectra presented below, excludes such a difference between regions with one- and two-layer graphene; therefore the observed variations cannot only be due to thickness changes. This is particularly true for regions of the surface with work function values of 4.46–4.49 eV. For these regions the C1s spectra (as discussed in the next section) indicate that the graphene film is in fact very thin.

There are also more substantial changes to the threshold spectra than the work function measurements suggest. To demonstrate this, Fig. 6(a) shows two examples of threshold spectra for regions of the sample with a small work function difference of  $\sim 30$  meV (4.42 and 4.45 eV). These regions will be analyzed in more detail using both core level X-PEEM and the  $k$ -PEEM data in the next sections. There are interesting variations in the structure of the secondary electron (SE) peak up to 4–5 eV above the vacuum level (i.e., above the photoemission threshold). The SE peak structure can be related to the conduction band.<sup>25</sup> Figure 6(b) shows the negative of the second derivative threshold spectra. The data have been smoothed in order to more clearly see the peak structure. The low work function regions in Fig. 5(c) have a single main structure in the SE at  $\sim 6.0$  eV whereas the higher work function regions have a clear double structure at  $\sim 6.0$  eV and  $\sim 7.50$  eV. The structure around 6 eV could be due to the bulk SiC bands observed along  $\Gamma A$ , which extend from 5.6 to above 6 eV.<sup>26</sup> Other conduction bands also disperse along the bulk directions  $ML$  and  $HK$ . In fact, all the high work function spectra show a double-peak structure in the SE whereas the low work function spectra show only one peak. This sort of SE structure has already been observed in threshold X-PEEM

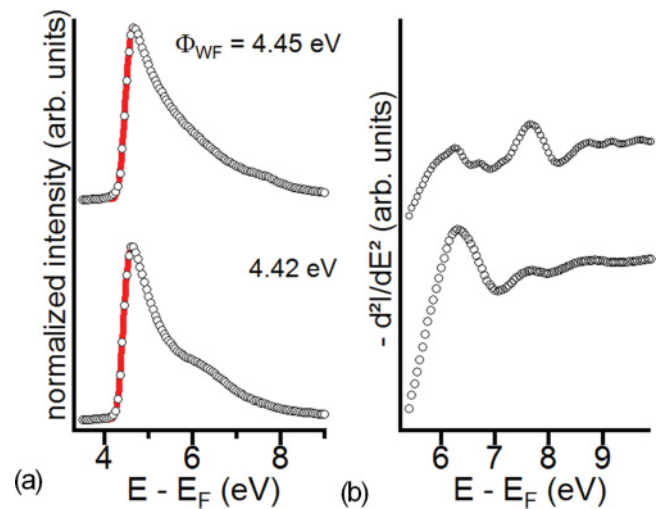


FIG. 6. (Color online) (a) Local threshold spectra extracted from regions in Fig. 5(b) with work functions of 4.42 and 4.45 eV. The best complementary error function fits of the rising edge of the photoemission threshold are indicated by the solid line. (b) Second derivative smoothed threshold spectra from (a) showing peaks corresponding to the empty conduction band structure.

analysis of graphene on SiC(0001).<sup>27</sup> It has been known for a long time that bulk graphite produces an intense secondary electron signal at 7.5 eV above the Fermi level (about 3 eV above the vacuum).<sup>28</sup> For example, the photocurrent carried by the Bloch constituent of the time-reversed LEED wave function is indeed a maximum near 7.5 eV.<sup>29</sup> Thus although the work function difference in Fig. 5(a) is small ( $\sim 30$  meV), we can identify the presence of a band at 7.5 eV, which for thicker samples could develop into the typical structure of graphite.

## 2. C1s core level

A series of energy filtered images have been acquired over the full C1s spectrum in the same FoV as the threshold data, allowing a pixel-by-pixel extraction of the local C1s spectra that can then be directly compared to the work function map. The C1s spectrum has two main components, one assigned to the SiC substrate near 283 eV, and the other to graphene near 285 eV.<sup>14</sup> Figure 7(a) shows a map of the total area of the SiC component. Because thicker graphene regions attenuate the photoelectrons from the SiC more, the map in Fig. 7(a) is a good estimate of the variations in the graphene thickness within the FoV. Comparison of the C1s intensity map with the work function map in Fig. 5(b) shows that there is no simple one-to-one correlation between graphene thickness and work function. Instead we will show that much of the contrast variations are a combination of both work function and core level spatial variations, indicating a complex chemical structure in the SiC-graphene interface.

In order to obtain more chemical-spatial detail, local, C1s core level spectra were extracted from each of the regions identified in Fig. 7 and are presented in Fig. 8. The graphene and SiC intensities show significant variations from one region to another, not only in total intensity but also in terms of the fine structure of both the graphene and SiC components. To fit

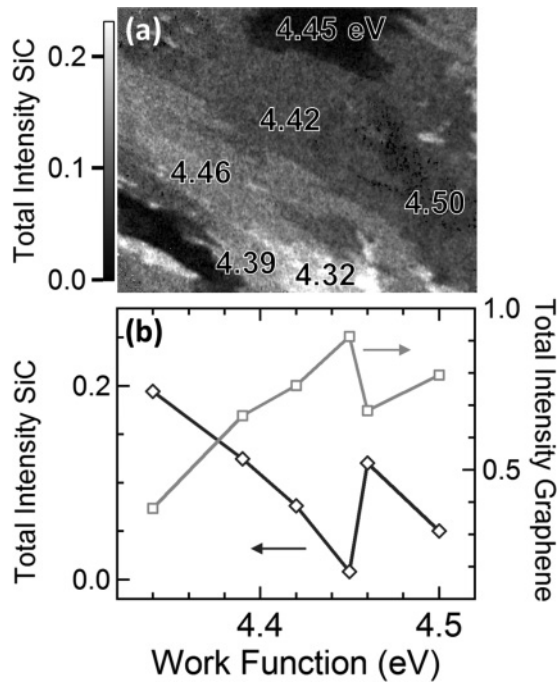


FIG. 7. (a) Intensity map (arbitrary units) of the SiC substrate component of C1s spectra after background subtraction. The darker regions correspond to lower intensity and therefore thicker graphene; FoV  $53 \mu\text{m}$ . (b) The C1s intensities from graphene (squares) and from SiC (diamonds) as a function of work function.

the spectra, we use five peaks, after subtraction of a Shirley background (a linear background fit was also tested but does not significantly change the results). Three components are necessary to fit the main peak of the spectrum that represents the graphene. For each of these components a Doniach-Sunjić line shape was used with a  $0.2 \text{ eV}$  Lorentzian width,  $0.3 \text{ eV}$  Gaussian width, and  $0.05$  asymmetry factor. A one-component Gaussian line shape (FWHM of  $0.5 \text{ eV}$ ) is used to fit the low binding energy peak ascribed to the SiC substrate. A Gaussian is more suitable for a wide-gap semiconductor. The binding energy of this component can vary by up to  $0.5 \text{ eV}$ . Finally, a small broad component, which is always present in the C1s spectrum around  $285.7 \text{ eV}$ , is ascribed to slight surface contamination due to residual gas in the vacuum chamber since the C1s image series were obtained  $1.3 \times 10^5 \text{ s}$  after the cleaning process. This peak was fitted using a Gaussian with a  $\text{FWHM} = 1.1 \text{ eV}$ . The contamination component increases slightly for thinner graphene, and is largest in the region with a work function of  $4.34 \text{ eV}$ . Immediately after cleaning, no such peak was visible. The  $k$ -PEEM data described below were obtained only  $\sim 10^4 \text{ s}$  after cleaning; thus the residual gas contamination in that case is expected to be negligible. The best fits are also reported in Fig. 8. Each spectrum is correlated with a region of the sample that is specified by its local work function and thickness (determined by the C1s intensities, as described below).

The main graphene component lies between  $284.30$  and  $284.56 \text{ eV}$  and is always the dominant contribution to the spectrum, confirming that there is graphene or a graphene-like layer over the whole film. This statement is supported by

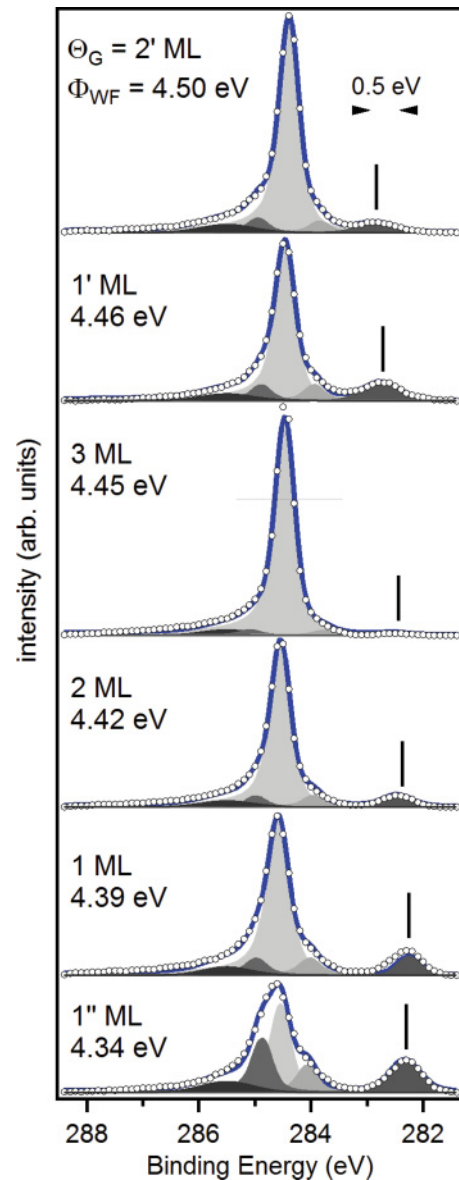


FIG. 8. (Color online) C1s core level spectra extracted from the regions shown in Fig. 7 together with the best 5-peak fits. The vertical lines indicate the position of the peak attributed to the SiC substrate. The main graphene peak is light gray, the contamination peak is in black, and the SiC component is dark gray. The two other graphene peaks, labeled HBE-G and LBE-G, flank the main graphene peak. The thickness (calibration is described in the text) and work function are given for each spectra.

the behavior of the SiC component, at lower binding energy. It is always much smaller than the main graphene component suggesting a nearly continuous graphene coverage. As the graphene intensity increases (i.e., the number of graphene layers increases), the intensity of the SiC decreases. We can estimate the local graphene thickness from the relative SiC and graphene C1s intensity. Using a graphene interlayer spacing of  $0.34$  and a  $1 \text{ nm}^{30}$  electron mean free path for  $654.3 \text{ eV}$  photons in graphite, the estimated attenuation of the substrate C1s signal is  $22\%$  per graphene layer. Assuming C atom surface densities for graphene ( $3.8 \times 10^{15} \text{ cm}^{-2}$ ) and SiC ( $1.22 \times 10^{15} \text{ cm}^{-2}$ ), the thickness of the graphene within the

TABLE I. C1s BE for the main graphene peak and for the SiC peak together, and the G/SiC core level intensity ratio for different graphene thicknesses and work functions.

Coverage (ML)	$\Phi_{WF}$ (eV)	C1s BE (eV)		Ratio $I_G/I_{SiC}$
		Graphene	Substrate	
3	4.45	284.45	282.52	112.3
2	4.42	284.55	282.46	10.0
2'	4.50	284.30	282.84	15.8
1	4.39	284.56	282.32	5.3
1'	4.46	284.45	282.75	5.7
1''	4.34	284.54	282.32	2.0

FoV is between 1 and 3 ML. This estimate is in agreement with the spread in the number of ML deduced from oscillations in the LEEM backscattered reflectivity curves. The thickness values obtained by this method are given in Fig. 8. The work function, C1s core level binding energies, and graphene thicknesses are summarized in Table I.

It is immediately obvious that there is not a simple one-to-one correspondence between work function and graphene coverage. The same graphene thickness is obtained in regions with significantly different work functions. We can group the six different contrast regions in Figs. 5(b) and 7(a) into three families. The first consists of graphene with 1, 2, or 3 layers. The second, denoted by a prime superscript, has either 1 or 2 ML graphene, while the third, denoted by a double prime, has only 1 ML graphene.

The complexity of the graphene-SiC interface is revealed by a detailed look at the C1s spectra in Fig. 8. There are always two other graphene-like peaks besides the main peak in all regions, a high binding energy (HBE-G) peak around 284.9 eV and a low binding energy (LBE-G) peak at 284.0. The intensity of these two peaks is lowest for 3 ML graphene and highest for the single-layer graphene, whatever the family. We therefore associate these two structures with carbon *below* the graphene layers, either in the C-terminating SiC layer or from some of the graphene at the SiC interface. Note that these HBE- and LBE-G peak intensities are not the same for the three single-layer graphene regions. They are most intense for the 1'' ML region, which also had the strongest SE structure associated with the SiC substrate. The 1 ML and 1'' ML graphene have similar C1s binding energies ( $\Delta BE = 100$  meV). The total work function variation over the three single-layer graphene regions is 120 meV. Similarly, 2 ML graphene has significant differences in its C1s binding energy and in its work function. The main graphene C1s peak BE in the 2' ML graphene is shifted 250 meV lower than the 2 ML graphene. At the same time, the SiC component shifts 380 meV to higher BE in the 2' ML. However, the work function difference between the 2 ML and 2' ML regions is 80 meV. The work function, C1s graphene, and SiC binding energies are plotted together in Fig. 9.

It follows that a uniform charge transfer over the whole graphene/SiC interface cannot be explained by these experimental observations. Charge transfer from the substrate to the graphene should result in a rigid shift of the electronic levels and the work function. However, in regions with the

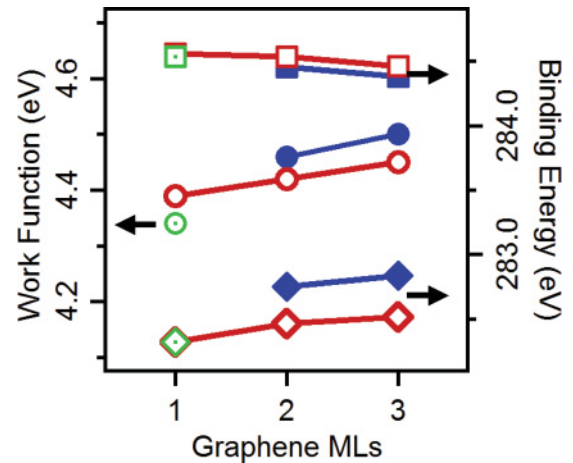


FIG. 9. (Color online) C1s graphene BE (squares), C1s SiC BE (diamonds), and work function (circles), as a function of graphene thickness. The unfilled symbols are for 1, 2, and 3 ML regions; filled symbols are for 1' and 2' ML regions. Open symbols with dots are for the 1'' ML.

same number of graphene layers we observe a spread in the work function. The work function difference between 1 ML and 1'' ML might be ascribed to the slightly higher surface contamination, but this cannot explain the work function and C1s BE difference with the 1' ML region which should have the same surface contamination. The most direct evidence for a nonuniform G/SiC interface is the shift of up to 220 meV in C1s SiC binding energy for different coverages. The trend in the SiC component binding energy emission is shown in Fig. 9. If we assume that the SiC C1s signal is dominated by the first substrate layer, the trend suggests two possible interfaces. Indeed, STM studies have shown that for very thin UHV grown graphene layers there are two different interface reconstructions ( $2 \times 2$  and  $3 \times 3$ ).<sup>15</sup> The BE variation of the C1s components as a function of thickness is also shown in Fig. 9. Different core level binding energies for the same graphene thickness further support the interpretation of a nonuniform G/SiC interface. Comparing the main G and SiC components, we see that as the SiC BE increases (charge transfer) there is a corresponding decrease in the G BE. Thus, the magnitude of the charge transfer depends on the local interface chemistry or structure.

### C. $k$ -PEEM results

In addition to the spatially resolved core level data, we are able to create local iso-intensity surfaces in  $(k_x, k_y, E)$  space. In this way, we can immediately visualize the full band dispersion in all directions parallel to the graphene planes for a selected micron-scale region. The objective is to correlate the chemical and electronic states obtained in X-PEEM with a quantitative analysis of the band structure of the same micron-scale region. Figure 10(a) shows a complete three-dimensional data set of the band dispersion near the Fermi level of the 2 ML region. The image series were taken from 2.9 eV below the Fermi level to 0.3 eV above  $E_F$  in 50 meV steps. The linearly polarized photon beam was incident at  $25^\circ$  with respect to the sample surface, giving a mainly  $p$ -polarized geometry in an arbitrary



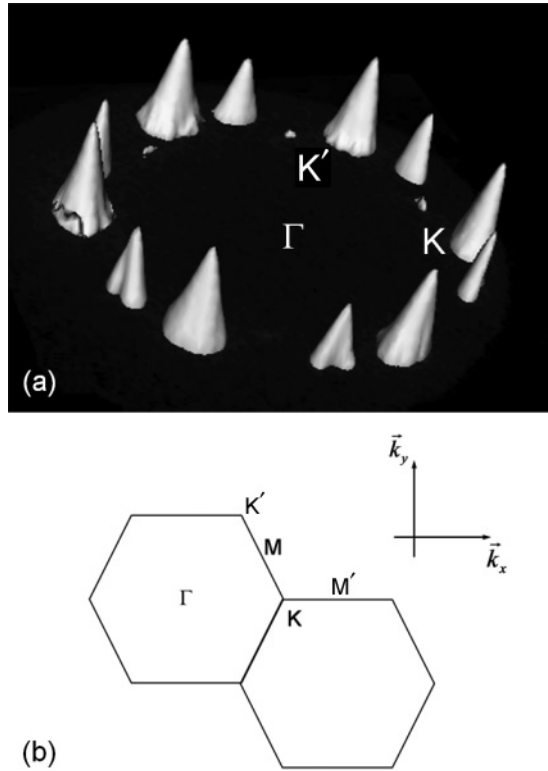


FIG. 10. (a) Experimental  $I(k_x, k_y, E)$  data collected in the 2 ML region of Fig. 7. The principal and secondary Dirac cones at the  $K$  and  $K'$  points of the first Brillouin zone are clearly visible. The secondary cones are rotated by  $21.9^\circ$  with respect to the primary cones. Also evident is the already documented suppression of the photoemission intensity outside the first Brillouin zone due to the pseudospin structure when using  $p$ -polarized light. The tertiary cones are just visible inside the double hexagon defined by the principal and secondary cones. (b) Schematic of the Brillouin zone of graphene showing the two high-symmetry directions parallel and perpendicular to  $\Gamma K M'$  ( $k_x$  and  $k_y$ , respectively) extracted from the  $k$ -PEEM data sets. An open source volume viewer, designed for medical imaging, was used to produce the image (Ref. 31).

azimuth ( $14.5^\circ$  off  $\Gamma K$ ). The acquisition of each image series took 22 minutes and they were repeated eight times in order to improve statistics without introducing camera noise.

Instead of the single set of six Dirac cones usually reported for Si-face films,<sup>32</sup> Fig. 10(a) shows three sets of Dirac cones, which we will call principal, secondary, and tertiary cones. The first two are much more intense than the latter. All three have the typical sixfold symmetry, although the tertiary cones appear inside the primary and secondary cone radius (i.e., at position  $< \Gamma K$ ). Also note the symmetry of the primary and secondary cones. They are not full circles because of the suppression of intensity in the second zone due to matrix element effects (an effect well known in graphene).<sup>32,33</sup> However, the tertiary cones have their symmetry flipped  $180^\circ$ . As we will demonstrate below, these three sets of cones are all due to two commensurately rotated graphene sheets.

The secondary Dirac cones have reciprocal lattice vectors  $*\Gamma K$  rotated by  $21.9^\circ$  with respect to the primary cones. This is very close to the value of  $21.8^\circ$  expected for a particular pair of commensurate rotated graphene sheets.<sup>35</sup> At first

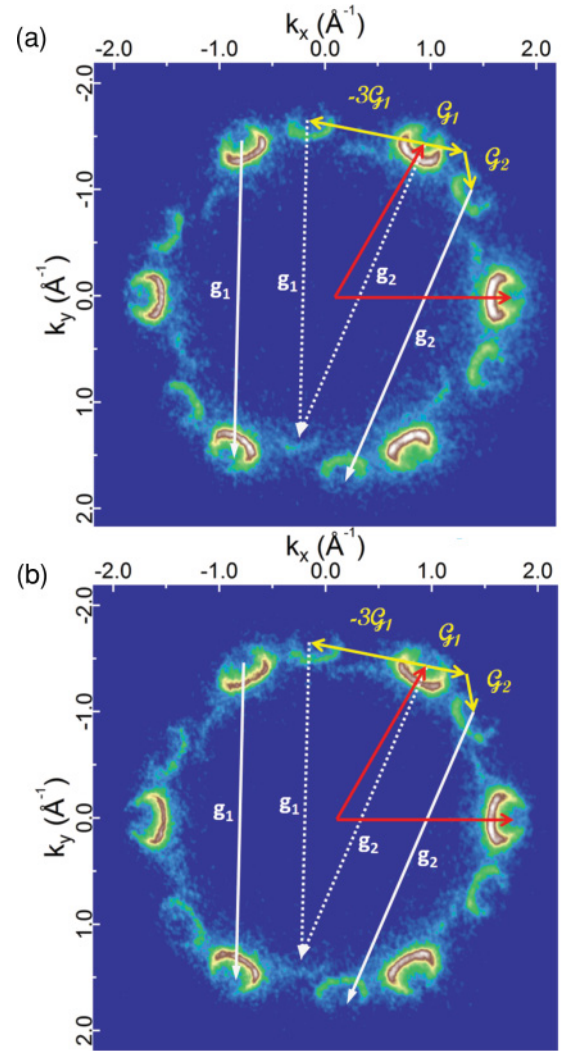


FIG. 11. (Color online) Horizontal slice in the 3D  $k$ -PEEM data set of (a) 2 ML and (b) 3 ML at a binding energy of 1.3 eV. Secondary Dirac cones (graphene reciprocal lattice constant  $g_1$ ) are rotated by  $21.9^\circ$  with respect to the principal cones (graphene reciprocal lattice constant  $g_2$ ). The tertiary cones are obtained by diffraction of either the secondary cone by the principal lattice vector  $g_1$  (dotted line), or by the primary cone by the secondary lattice vector  $g_2$  (dotted line). The tertiary cones are stronger in 2 ML graphene.

sight, one would be tempted to interpret the tertiary cones in terms of replicas, like those observed on the SiC(0001) Si face.<sup>34</sup> However, those replicas are due to registry between the  $(6\sqrt{3} \times 6\sqrt{3})R30^\circ$  reconstructed substrate and the graphene overlayer. On SiC(000 $\bar{1}$ ) the graphene layers are known to form commensurate rotated layers where the average rotation between pairs is  $30^\circ \pm \sim 7^\circ$ .<sup>5</sup> The tertiary cones in Fig. 11 are instead due to a diffraction effect caused by the supercell formed by the commensurate rotations. To understand this, note that the supercell formed by the stacked rotated sheets is defined by reciprocal lattice vectors  $\vec{G}_1$  and  $\vec{G}_2$ . These supercell vectors are, in turn, an integer sum of the primary graphene reciprocal vectors,  $\vec{g}_{1a}$ ,  $\vec{g}_{1b}$ ,  $\vec{g}_{2a}$ , and  $\vec{g}_{2b}$ , from the two layers (i.e.,  $\vec{G}_1 = p\vec{g}_{1a} + q\vec{g}_{1b}$  and  $\vec{G}_2 = p'\vec{g}_{2a} + q'\vec{g}_{2b}$ , where  $p$ ,  $q$ ,  $p'$ , and  $q'$  are integers).<sup>35</sup>

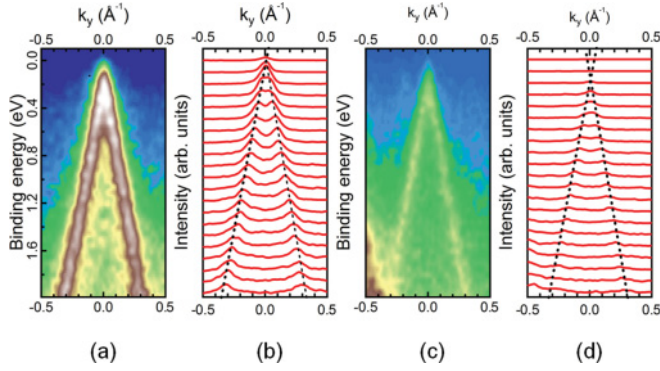


FIG. 12. (Color online) Band dispersion as a function of  $k_y$  around the  $K$  point at the first Brillouin zone boundary observed in the 3ML region for (a) principal and (c) secondary cones. The respective momentum distribution curves over the same energy range are shown in (b) and (d). The peak positions are highlighted by the dotted lines showing the variation in the position of the Dirac point for successive graphene layers.

In Fig. 11, we show two examples where two of the secondary cones are separated by linear sums of lattice vectors  $\vec{G}_1$  and  $\vec{G}_2$ , i.e.,  $-3\vec{G}_1$  and  $-(\vec{G}_1 + \vec{G}_2)$ . Note that  $(\vec{G}_1 + \vec{G}_2) = (\vec{g}_{1a} - \vec{g}_{2a})$ , indicating that the two rotated graphene sheets are indeed a commensurate rotated pair. For the purpose of discussion, we use the notation that  $\vec{g}_1$ 's are the graphene lattice vectors of the primary cones and  $\vec{g}_2$ 's are the graphene lattice vectors of the secondary cones. Using this notation, it is easy to show that the tertiary cones are diffracted replicas of the primary and secondary cones. Figure 11 shows that a tertiary cone is formed by diffracting a primary cone by  $\vec{g}_2$  or a secondary cone by  $\vec{g}_1$ . This diffraction process explains why the tertiary cones are rotated by  $180^\circ$  relative to the primary and secondary cones; they are simply translated Dirac cones from a  $K$  and  $K'$  point of one lattice by the  $\vec{g}$  of the second lattice. Because any tertiary cones can be formed by diffraction of either of the rotated graphene lattices (primary or secondary), the two rotated graphene sheets must be stacked on top of each other with a commensurate rotation. Separated rotated sheets cannot give rise to this type of diffraction.

The  $\pi$  bands of the primary cones cross at a Dirac point of 0.30 eV for the 2 ML film and 0.25 eV for the 3 ML film relative to the Fermi level. Figure 12 shows cuts perpendicular to  $\Gamma KM$  of the primary and secondary cones for 3 ML. The linear dispersion of the  $\pi$  band near the Dirac point is evident. Panels (a) and (c) show the raw experimental data around the  $K$  point of the Dirac cones. Panels (b) and (d) show the corresponding momentum distribution curves (MDCs) extracted from the data. The Fermi level calibration was checked by extracting the local spectra from a small zone around the Dirac cones. This has the advantage of minimizing noise and thus allowing a more precise location of the Fermi level. The dotted lines show that the  $\pi$  bands cross at a Dirac point 50–75 meV closer to the Fermi level for the principal cones. The group velocity of the quasiparticle is  $(1.05 \pm 0.05) \times 10^6$  m s $^{-1}$  in both 2 ML and 3 ML regions.

This confirms that the electron doping is a function of film thickness and is consistent with the results for graphene on

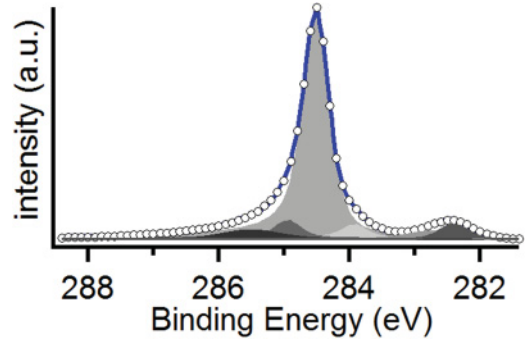


FIG. 13. (Color online) Area averaged C1s core level spectrum. The average is over the 53  $\mu\text{m}$  FoV.

the Si face where the charge transfer induced shift of the band structure is greater for thinner films.<sup>36</sup>

#### IV. CONCLUSION

We have studied spatial variations in and correlations between the work function, chemical states, and electronic states of few-layer graphene grown epitaxially on SiC(000 $\bar{1}$ ). These experiments demonstrate that near uniformly thick graphene films can be prepared using the CCS growth method; in this sample more than 80% of the surface is 2–3 layers thick. More importantly, they also show that while LEEM can be used to give local information on the graphene film's thickness, LEEM contrast variation on C-face graphene films is not simply due to film thickness alone. X-PEEM's spatial resolution has proven to be very useful in illuminating the origin of these contrast variations. The 0.1  $\mu\text{m}$  spatial resolution in the present experiment is much better than that currently obtained in area-averaged high-resolution ARPES with synchrotron radiation. The work function variations in Fig. 5, derived from the X-PEEM, combined with the local C1s spectra in Fig. 8, show an interface chemistry that is more complex than originally suspected.

To demonstrate this, Fig. 13 shows an area-averaged C1s spectrum from the 53  $\mu\text{m}$  FoV. The overall spectrum is broader, and the fine structure visible in the local spectra of Fig. 8 is smeared out in the area-averaged spectrum. Without the spatial resolution, one would have concluded that only one broad substrate peak was present rather than a narrower peak whose energy shift depends on the graphene thickness. Similarly, the area-averaged work function masked the complexity of charge transfer at the graphene-SiC interface.

While the X-PEEM data agree with the general trend observed by others that the work function tends to higher values with thicker graphene films, it shows that the situation is more complicated. For a given thickness, both the local work function and C1s BE vary appreciably. The data suggest that at least two SiC terminations with different local bonding appear to be present at the interface. We note that the long-range order of these different bonding areas is not very high since the micro-LEED never sees any superlattice diffraction spots. For a given graphene-SiC interface, the core level data can be interpreted within the framework of a charge transfer model between the substrate and the graphene that rigidly shifts the

C1s core level. The effect of the charge transfer on binding energy is greater for carbon closer to the interface, i.e., for carbon in thinner graphene films. The correlation between the work function and the core level BE strongly supports this interpretation. On the basis of these results we suggest that there are two distinct interfacial chemical regions.

There are several possible reasons for these two distinct regions. It is known that UHV grown C-face graphene can have a  $2 \times 2$  and  $3 \times 3$  interface phases coexisting.<sup>15</sup> The structures are thought to have very different binding configurations with the graphene. While no reconstructions are observed in LEED on our samples, the high growth temperatures encountered during furnace growth (1550 °C versus 1100 °C) may cause these regions to be very disordered. Nonequilibrium local Si concentrations may also be the cause of the different interface regions. Because Si diffusion (a required step for graphene growth) is difficult through graphene, local defect driven Si outflow may increase or decrease the interfacial Si concentration in different regions of the sample. It is clear that more experimental work needs to be done to resolve this issue, notably imaging of the Si  $2p$  core levels. Experiments are now being planned for such studies.

We have also demonstrated that  $k$ -PEEM gives detailed band structure information from commensurately rotated

graphene sheets. The easy switching between real- and  $k$ -space imaging modes allows, within the limits of the spatial resolution and field aperture size, correlation between the chemical and electronic states of the surface and graphene-SiC interface. In this study we conclusively show that commensurately rotated graphene pairs exist.

## ACKNOWLEDGMENTS

C.M. benefited from a grant of the Nanosciences programme of the French Atomic and Alternative Energy Authority. J.R. is funded by a CEA Ph.D. grant Contrat de Formation par la recherche. The work was supported by the French National Research Agency (ANR) through the Recherche Technologique de Base (RTB) program. We acknowledge SOLEIL for provision of synchrotron radiation facilities, and we would like to thank F. Sirotti, the TEMPO beamline staff, D. Martinotti, B. Delomez, and F. Merlet for technical assistance. E.C., W.A.d.H., and C.B. would like to acknowledge support from the W. M. Keck Foundation, the Partner University Fund from the Embassy of France, and the NSF under Grant No. DMR-0820382. E.C. would also like to acknowledge additional support from the NSF under Grant No. DMR-1005880.

\*Correspondence should be addressed to nick.barrett@cea.fr

<sup>1</sup>J. S. Moon, D. Curtis, M. Hu, D. Wong, C. McGuire, P. M. Campbell, G. Jernigan, J. L. Tedesco, B. VanMil, R. Myers-Ward, C. Eddy Jr., and D. K. Gaskill, *IEEE Electron Device Lett.* **30**, 650 (2009).

<sup>2</sup>Yu-Ming Lin, K. A. Jenkins, A. Valdes-Garcia, J. P. Small, D. B. Farmer, and P. Avouris, *Nano Lett.* **9**, 422 (2009).

<sup>3</sup>C. Riedl, C. Coletti, and U. Starke, *J. Phys. D: Appl. Phys.* **43**, 374009 (2010).

<sup>4</sup>W. A. de Heer, C. Berger, M. Ruan, M. Sprinkle, X. Li, Y. Hu, B. Zhang, J. Hankinson, and E. H. Conrad, e-print arXiv:1104.1359 [cond-mat].

<sup>5</sup>M. Sprinkle, D. Siegel, Y. Hu, J. Hicks, A. Tejada, A. Taleb-Ibrahimi, P. Le Fèvre, F. Bertran, S. Vizzini, H. Enriquez, S. Chiang, P. Soukiassian, C. Berger, W. A. de Heer, A. Lanzara, and E. H. Conrad, *Phys. Rev. Lett.* **103**, 226803 (2009).

<sup>6</sup>J. Hass, F. Varchon, J. E. Millan-Otoya, M. Sprinkle, N. Sharma, W. A. de Heer, C. Berger, P. N. First, L. Magaud, and E. H. Conrad, *Phys. Rev. Lett.* **100**, 125504 (2008).

<sup>7</sup>C. Berger, Z. Song, X. Li, X. Wu, N. Brown, C. Naud, D. Mayou, T. Li, J. Hass, A. N. Marchenkov, E. H. Conrad, P. N. First, and W. A. de Heer, *Science* **312**, 1191 (2006).

<sup>8</sup>M. Orlita, C. Faugeras, P. Plochocka, P. Neugebauer, G. Martinez, D. K. Maude, A.-L. Barra, M. Sprinkle, C. Berger, W. A. de Heer, and M. Potemski, *Phys. Rev. Lett.* **101**, 267601 (2008).

<sup>9</sup>J. Hass, W. A. de Heer, and E. H. Conrad, *J. Phys. Condens. Matter* **20**, 323202 (2008).

<sup>10</sup>C. Riedl, C. Coletti, T. Iwasaki, A. A. Zakharov, and U. Starke, *Phys. Rev. Lett.* **103**, 246804 (2009).

<sup>11</sup>U. Starke and C. Riedl, *J. Phys. Condens. Matter* **21**, 134016 (2009).

<sup>12</sup>J. Hass, J. E. Millán-Otoya, P. N. First, and E. H. Conrad, *Phys. Rev. B* **78**, 205424 (2008).

<sup>13</sup>J. Hass, R. Feng, J. E. Millan-Otoya, X. Li, M. Sprinkle, P. N. First, W. A. de Heer, E. H. Conrad, and C. Berger, *Phys. Rev. B* **75**, 214109 (2007).

<sup>14</sup>K. V. Emtsev, F. Speck, Th. Seyller, L. Ley, and J. D. Riley, *Phys. Rev. B* **77**, 155303 (2008).

<sup>15</sup>F. Hiebel, P. Mallet, F. Varchon, L. Magaud, and J.-Y. Veullen, *Phys. Rev. B* **78**, 153412 (2008).

<sup>16</sup>Luxmi, N. Srivastava, Guowei He, R. M. Feenstra, and P. J. Fisher, *Phys. Rev. B* **82**, 235406 (2010).

<sup>17</sup>B. Krömker, M. Escher, D. Funnemann, D. Hartung, H. Engelhard, and J. Kirschner, *Rev. Sci. Instrum.* **79**, 053702 (2008).

<sup>18</sup>M. Escher, N. Weber, M. Merkel, C. Ziethen, P. Bernhard, G. Schonhense, S. Schmidt, F. Forster, F. Reinert, B. Krömker, and D. Funnemann, *J. Phys. Condens. Matter* **17**, S1329 (2005).

<sup>19</sup>M. Escher, K. Winkler, O. Renault, and N. Barrett, *J. Electron Spectrosc. Relat. Phenom.* **178–179**, 303 (2010).

<sup>20</sup>H. Hibino, H. Kageshima, F. Maeda, M. Nagase, Y. Kobayashi, and H. Yamaguchi, *Phys. Rev. B* **77**, 075413 (2008).

<sup>21</sup>T. Ohta, F. El Gabaly, A. Bostwick, J. L. McChesney, K. V. Emtsev, A. K. Schmid, T. Seyller, K. Horn, and E. Rotenberg, *New J. Phys.* **10**, 023034 (2008).

<sup>22</sup>W. F. Chung, Y. J. Feng, H. C. Poon, C. T. Chan, S. Y. Tong, and M. S. Altman, *Phys. Rev. Lett.* **90**, 216105 (2003).

<sup>23</sup>O. Renault, R. Brochier, A. Roule, P.-H. Haumesser, B. Krömker, and D. Funnemann, *Surf. Interface Anal.* **38**, 375 (2006).

<sup>24</sup>T. Filleter, K. V. Emtsev, Th. Seyller, and R. Bennewitz, *Appl. Phys. Lett.* **93**, 133117 (2008).

- <sup>25</sup>R. Feder and J. B. Pendry, *Solid State Commun.* **26**, 529 (1978).
- <sup>26</sup>C. Persson and U. Lindefelt, *J. Appl. Phys.* **82**, 5496 (1997).
- <sup>27</sup>H. Hibino, H. Kageshima, M. Kotsugi, F. Maeda, F.-Z. Guo, and Y. Watanabe, *Phys. Rev. B* **79**, 125437 (2009).
- <sup>28</sup>R. F. Willis, B. Feuerbacher, and B. Fitton, *Phys. Rev. B* **4**, 2441 (1971).
- <sup>29</sup>N. Barrett, E. E. Krasovskii, J.-M. Themlin, and V. N. Strocov, *Phys. Rev. B* **71**, 035427 (2005).
- <sup>30</sup>S. Tanuma, C. J. Powell, and D. R. Penn, *Surf. Interface Anal.* **17**, 911 (1991).
- <sup>31</sup>The program may be downloaded at [<http://microview.sourceforge.net/>].
- <sup>32</sup>A. Bostwick, T. Ohta, T. Seyller, K. Horn, and E. Rotenberg, *Nature Phys.* **3**, 36 (2007).
- <sup>33</sup>E. L. Shirley, L. J. Terminello, A. Santoni, and F. J. Himpsel, *Phys. Rev. B* **51**, 13614 (1995).
- <sup>34</sup>K. Nakatsuji, Y. Shibata, R. Niikura, F. Komori, K. Morita, and S. Tanaka, *Phys. Rev. B* **82**, 045428 (2010).
- <sup>35</sup>E. J. Mele, *Phys. Rev. B* **81**, 161405(R) (2010).
- <sup>36</sup>T. Ohta, A. Bostwick, J. L. McChesney, T. Seyller, K. Horn, and E. Rotenberg, *Phys. Rev. Lett.* **98**, 206802 (2007).